Properties of the shear stress peak radiated ahead of rapidly accelerating rupture fronts that mediate frictional slip

Ilya Svetlizky[a], Daniel Pino Muñoz[b], Mathilde Radiguet[b], David S. Kammer[a], Jean-François Molinari[b], and Jay Fineberg[a,1]

[a]The Racah Institute of Physics, The Hebrew University of Jerusalem, Givat Ram, Jerusalem 91904, Israel; and [b]Civil Engineering Institute, Materials Science and Engineering Institute, Ecole Polytechnique Fédérale de Lausanne, Station 18, CH-1015 Lausanne, Switzerland

Edited by David A. Weitz, Harvard University, Cambridge, MA, and approved November 30, 2015 (received for review September 2, 2015)

We study rapidly accelerating rupture fronts at the onset of frictional motion by performing high-temporal-resolution measurements of both the real contact area and the strain fields surrounding the propagating rupture tip. We observe large-amplitude and localized shear stress peaks that precede rupture fronts and propagate at the shear-wave speed. These localized stress waves, which retain a well-defined form, are initiated during the rapid rupture acceleration phase. They transport considerable energy and are capable of nucleating a secondary supershear rupture. The amplitude of these localized waves roughly scales with the dynamic stress drop and does not decrease as long as the rupture front driving it continues to propagate. Only upon rupture arrest does decay initiate, although the stress wave both continues to propagate and retains its characteristic form. These experimental results are qualitatively described by a self-similar model: a simplified analytical solution of a suddenly expanding shear crack. Quantitative agreement with experiment is provided by realistic finite-element simulations that demonstrate that the radiated stress waves are strongly focused in the direction of the rupture front propagation and describe both their amplitude growth and spatial scaling. Our results demonstrate the extensive applicability of brittle fracture theory to fundamental understanding of friction. Implications for earthquake dynamics are discussed.

nonsteady rupture dynamics | acoustic radiation | friction | earthquake dynamics | seismic radiation

The onset of motion along a frictional interface entails rupture-front propagation. These rupture fronts have long been considered to have much in common with propagating cracks (1–3). Recent friction experiments (4) have shown that the stresses and material motion surrounding the tip of a propagating rupture are indeed quantitatively described by singular linear elastic fracture mechanics (LEFM) solutions originally developed for brittle shear fracture. These singular fields are only regularized by dissipative and nonlinear processes in the vicinity of the rupture tip.

Nonsteady processes such as rapid rupture velocity variation during the nucleation or arrest phases result in the generation of stress-wave radiation (2, 5). In the study of earthquakes, understanding the source mechanism of those waves is of primary importance. Long-wavelength radiation is usually described by simple dislocation models (3, 6). High-frequency radiation, however, was proposed (2) to be controlled by the strong slip velocity concentrations at the rupture tip predicted by fracture mechanics. Descriptions that go beyond singular contributions to fracture involve significant analytical complications; full solutions of nonsteady dynamic crack problems are generally extremely difficult to obtain. Of the few full-field analytic solutions available, self-similar solutions of suddenly expanding shear cracks have provided much intuition (2, 5, 7, 8). These solutions, under shear loading (mode II), predict a localized shear stress peak that propagates ahead of the rupture tip at the shear-wave velocity. The results obtained in such solutions are generally considered as an upper bound for the realistic stress-wave radiation of smoothly accelerating ruptures. Radiated shear stress peaks have, for decades, drawn special attention, because they are thought to be an important vehicle for the nucleation of supershear ruptures, a class of ruptures that propagate beyond the shear-wave speed, C_S. These ruptures surpass the Rayleigh wave speed, C_R, the classic "speed limit" for rapid singular cracks. This idea was first postulated in ref. 1 and later numerically observed in ref. 9, who found that a sufficiently strong shear stress peak can overcome interfacial strength and nucleate a daughter crack that will propagate at supershear velocities (10–15). Such supershear ruptures have indeed been observed along natural fault planes (16, 17) and in laboratory experiments (18–21).

Despite their importance, experimental studies of radiated stress waves have been very limited. Here we present direct measurements of the stress fields surrounding the tips of rapidly propagating ruptures and show how a shear stress peak is formed. Supplementing experiments with finite-element calculations, we provide a detailed description of both the scaling and space–time structure of this phenomenon.

Experimental Observations

Our experimental system is schematically presented in Fig. 1*A*. Two poly(methylmethacrylate) blocks with ~1-μm rough surfaces are pressed together by an external normal force, F_N (2–6 MPa nominal pressure). Shear and longitudinal velocities are, respectively, $C_S = 1{,}345$ m/s and $C_L = 2{,}333$ m/s (plane stress). The

Significance

The transition from stick to slip is governed by rupture fronts propagating along a frictional interface. It has long been suggested that rapid acceleration of these ruptures generates a shear stress peak that propagates ahead of the front. These peaked waves are strong; they can reach amplitudes that are large enough to trigger secondary supershear ruptures. We provide the first extensive quantitative experimental study to our knowledge of these highly directed waves and their relation to the rupture fronts driving them. Combining our experiments with finite-element simulations, we observe how these waves scale. This study provides insight into how rupture fronts accelerate beyond the shear-wave speed and may offer a possibility to obtain illusive information about propagating earthquakes.

Author contributions: J.-F.M. and J.F. designed research; I.S. performed the experimental work; D.P.M., M.R., and D.S.K. performed the numerical work; and I.S., D.P.M., M.R., D.S.K., J.-F.M., and J.F. contributed to analysis of the data and to writing the paper.

The authors declare no conflict of interest.

This article is a PNAS Direct Submission.

[1]To whom correspondence should be addressed. Email: jay@vms.huji.ac.il.

This article contains supporting information online at www.pnas.org/lookup/suppl/doi:10.1073/pnas.1517545113/-/DCSupplemental.

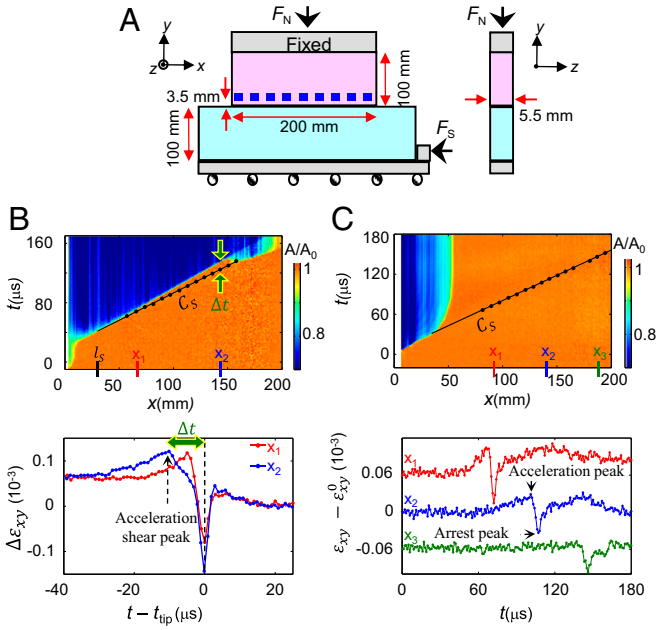

Fig. 1. Prominent shear stress peaks due to accelerating or suddenly arrested frictional rupture fronts. (*A*) Nineteen rosette strain gauges (blue squares), mounted at $y \sim 3.5$ mm measure the three 2D strain tensor components simultaneously every 1 μs. These are synchronized with real contact area, $A(x,t)$, measurements. (*B*, *Top*) $A(x,t)$ evolution (normalized at nucleation time, $t = 0$), along the quasi-1D interface due to a rupture front that nucleated at $x \sim 0$, rapidly accelerated to $\sim C_R$, and transitioned to supershear at $x \approx 155$ mm. (*Bottom*) Shear strain variations, $\Delta\varepsilon_{xy} = \varepsilon_{xy} - \varepsilon^r_{xy}$, relative to the rupture tip arrival time, t_{tip}, at the two locations, x_1 (red) and x_2 (blue) denoted above, show prominent amplitude shear strain peaks preceding the rupture tip arrival. For simplicity, we refer to these peaks as "shear stress peaks." ε^r_{xy} are residual values after the rupture front's passage. Successive measurements (black points in upper panel) reveal that these peaks propagate at C_S, and trigger supershear rupture. (*C*) Measurements of ε_{xy} (*Bottom*) and the contact area (*Top*) reveal an inverted shear peak propagating at C_S long after rupture arrest. Extrapolation (solid line) indicates that its origin coincides with rupture arrest. Arrest is due to decreasing values of ε^0_{xy} with x (22, 24). (*Bottom*) ε_{xy} measurements at three spatial points denoted above. The red (green) y axis is shifted by $0.06 \cdot 10^{-3}$ ($-0.06 \cdot 10^{-3}$) relative to initial values, ε^0_{xy}, for clarity. Black points in upper panels are measured peak locations.

complete 2D strain tensor, ε_{ij}, is measured at 19 locations along and ~3.5 mm above the frictional interface ($y = 0$) separating the blocks. Each strain component is measured at rates of 1 million samples per second. All strain measurements are local (each three-component strain gauge is 1×1 mm in size). Concurrent high-spatial-resolution measurements of the real area of contact, $A(x,t)$ (x being the coordinate along the quasi-1D frictional interface), are obtained at 580,000 frames per second by means of direct optical imaging of $A(x,t)$ along the entire 200×5.5-mm frictional interface (4). More details are given in *Supporting Information*. Once F_N is fixed, the shear force, F_S, is applied quasistatically by slowly incrementing F_S until the transition from stick to slip occurs.

The onset of frictional motion is marked by propagating crack-like rupture fronts that leave in their wake significantly reduced $A(x,t)$ (4, 20). We define the location of the rupture tip as the point where a sharp reduction of $A(x,t)$ occurs (orange to blue boundaries in Fig. 1). A typical example of a rupture front, asymptotically accelerating to rupture velocities, $C_f \to C_R$ (~1,237 m/s), is presented in Fig. 1*B*, *Top*.

In what follows we consider the strain fields surrounding the propagating rupture. Owing to the linearity of the governing equations, constant values of the initial tensile strains ε^0_{xx}, ε^0_{yy} and the residual frictional level on the crack faces, ε^r_{xy}, can be subtracted without loss of generality (3). We define strain variations, $\Delta\varepsilon_{ij}$, with respect to these initial and residual strains. The corresponding stress variations, $\Delta\sigma_{ij}$, can be calculated (under plane stress hypothesis). In what follows σ_{ij} and ε_{ij} are used interchangeably.

Fig. 1*B*, *Bottom* presents temporal measurements of shear strain variations, $\Delta\varepsilon_{xy}$, at two spatially separated locations along the frictional interface. Both signals are presented relative to the rupture tip arrival time, t_{tip}. It is evident that prominent peaks in the shear strain component precede the rupture tip arrival. For simplicity, we will refer to these peaks as "shear stress peaks," although they will, at times, be presented as peaks in the strain. Analysis of peak arrival times (e.g., Fig. 1*B*, *Top*) reveals that they propagate at C_S as they progressively distance themselves from the rupture tips that created them. Extrapolating the space–time peak trajectories to the intersection point with the rupture trajectory implies that the initiation of this radiated stress wave does not coincide with the rupture nucleation point ($x \approx 0$) but that it appears in the later stages of the accelerating phase. This is a general feature of all of the observed ruptures.

The measurements of $A(x,t)$ presented in Fig. 1*B* reveal the sudden nucleation ($x \approx 155$ mm) of a secondary supershear rupture front (propagating at $C_f > C_S$). The synchronized measurements of ε_{xy} and $A(x,t)$ provide direct evidence that the supershear rupture was triggered by the arrival of the shear stress peak. This type of transition is not uncommon.

Overall relative motion of the two blocks occurs only after a rupture front has traversed the entire interface. Rupture fronts may arrest (Fig. 1*C*, *Top*), however, if they encounter either reduced shear stress regions or areas of increased interfacial strength (22–24). Measurements of ε_{xy} (Fig. 1*C*, *Bottom*) indicate that the shear stress peak in Fig. 1*B*, in fact, persists, propagating far beyond the rupture arrest location while broadening and decaying in time. In addition, an inverted shear stress peak is generated that propagates at C_S with its origin at the initial stages of the arrest phase (Fig. 1*C*, *Top*). This inverted shear stress peak is not to be confused with the violent oscillation at the rupture tip in Fig. 1*B*, *Bottom*. These experimental observations confirm predictions (2) that the nucleation and arrest stress-wave radiation are complementary phenomena, having the same form but with inverted signs.

The examples above demonstrate the general notion that generation of stress-wave radiation requires nonsteady rupture processes. Let us now consider the explicit form of this radiation. In some simplified cases, analytical solutions are available (5) that describe radiation patterns generated by accelerating shear cracks. One such solution (7, 8) describes bilaterally expanding ruptures that initiate with zero initial length and propagate at a constant velocity ($C_f < C_R$) under uniform remote shear stress (Fig. 2*A*). In this problem, there is no characteristic time or length scale so self-similar propagating solutions can be found (*Supporting Information*). We will call this the "self-similar" solution, which was derived both for tension (25) and shear (1). The resulting normalized shear strain on the interface ($y = 0$) is plotted in Fig. 2*A*, *Bottom*. This solution describes a singular propagating crack tip that is preceded by a sharp and relatively localized shear stress peak. In crack tip vicinities all stress components (and strains) have the universal singular form $\sigma_{ij} \sim r^{-1/2}$ (7). This singular contribution dominates the near-tip stress fields in brittle fracture. The proportionality factor of the singularity (the stress intensity factor) depends on the fracture energy, Γ (the energy dissipated per unit crack advance). Whereas Γ generally depends on the material constitutive law, a consequence of the self-similar solution is that Γ must linearly increase with the propagation distance, l (26).

Experiments (4) have shown that under low shear stress loading, σ^0_{xy}, the strain components surrounding the tip of slowly

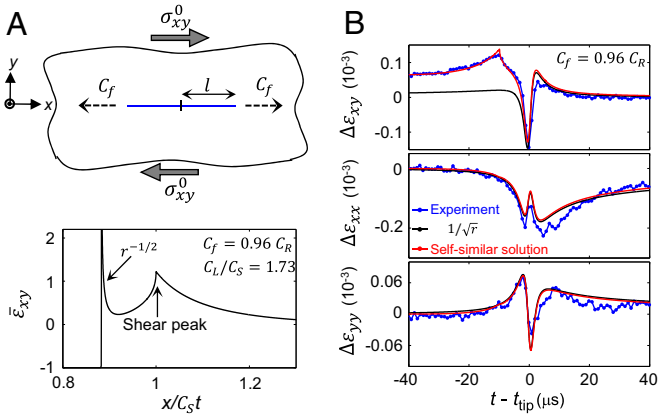

Fig. 2. Comparison of measured $\Delta\varepsilon_{ij}$ with the self-similar solution. (*A*, *Top*) We consider a self-similar bilaterally expanding rupture initiating at zero initial length and propagating at a constant rate under uniform remote shear stress, σ^0_{xy}, and residual frictional shear stress, σ^r_{xy}. The propagation length is given by $l = C_f t$. (*Bottom*) Close-up of the self-similar solution, $\bar{\varepsilon}_{xy} = (\varepsilon_{xy} - \varepsilon^0_{xy})/(\varepsilon^0_{xy} - \varepsilon^r_{xy})$, at $y = 0$ shows a pronounced shear stress peak propagating ahead of the singular rupture tip. (*B*) Comparison of $\Delta\varepsilon_{ij}$ measured at $y = 3.5$ mm, $x = x_2$ (blue) during a rupture event of Fig. 1*B* with both the singular LEFM predictions and the self-similar solution. Time is relative to the rupture tip arrival, t_{tip}. The singular term of the LEFM solution is plotted in black ($C_f = 0.96 C_R$, $\Gamma = 0.6$ J/m^2). Although it captures $\Delta\varepsilon_{xx}$ and $\Delta\varepsilon_{yy}$ well, the singular term fails to describe $\Delta\varepsilon_{xy}$ for $t - t_{tip} < 0$. Shown in red, the corresponding self-similar solution [$C_f = 0.96 C_R$, $\varepsilon^0_{xy} - \varepsilon^r_{xy} \approx 0.06 \cdot 10^{-3}$, $l = 100$ mm result in $\Gamma(l = 100\ \text{mm})$ J/m^2] entirely captures all measured strain components including the initial shear strain, ε^0_{xy}, and the shear stress peak far before the rupture tip arrival. The difference in $\Delta\varepsilon_{xy}$ in the two solutions highlights the importance of nonsingular contributions.

propagating frictional ruptures, are well-described by the universal singular form. Γ, the sole free parameter in this description, was shown to be constant, roughly independent of both C_f and the propagation distance. When $C_f \to C_R$, however, the singular form fails to describe $\Delta\varepsilon_{xy}$ measurements for $t - t_{tip} < 0$ (4), as demonstrated in Fig. 2*B*.

Fig. 2*B* also shows that the self-similar solution of an expanding shear rupture can describe all of the measured strain components rather well. In particular, this solution can capture both the initial shear loading, σ^0_{xy}, as well as the propagating shear stress peak far before the rupture tip arrival. We expect (Fig. S1) significant contributions due to the shear stress peak in measurements of the interface normal component of the particle velocity. This demonstrates the importance of the nonsingular contributions to strains at finite distances from the rupture front tip (27). The solution highlights the underlying physical picture: Rapid rupture front acceleration (mimicked by infinite acceleration in the self-similar problem) results in radiation in the form of a localized shear stress peak propagating at C_S.

The fact that the form of the solution is so close to experiment suggests that the general form of the radiation pattern may be captured by this solution, but one should be careful not to take this comparison too far. The self-similar problem is, in many respects, unphysical; its core assumptions include a constant rupture front velocity propagating under constant background stress that yields a continually increasing Γ with l. None of these is generally satisfied in the experiments. To perform the comparison in Fig. 2*B* we needed to choose both l and C_f in the model to correspond to the measured Γ and the instantaneous rupture velocity (*Supporting Information*). Although the self-similar problem might, consequently, be unrealistic (but see ref. 28), it nevertheless provides important physical intuition and has often been used to verify numerical methods (26).

Finite-Element Simulations

To make quantitative comparisons with the experiments, we performed 2D finite-element calculations in which the plane-stress hypothesis, block dimensions, and their elastic moduli correspond to the experimental system. The experimental loading configuration is mimicked by applying homogeneous shear and normal stresses (Fig. 3*A*, *Inset*). To close the system, we choose the widely used (9, 13, 14, 23) linear slip weakening friction law. This is the simplest cohesive zone model that captures both measurements (4) of Γ and the dissipation zone size [where the singular fields are regularized (3)]. Element rupture occurs when the shear stress on the interface, $\sigma_{xy}(y = 0)$, reaches an upper yield stress, σ^p_{xy}(5.3 MPa). Once local relative slip between the upper and bottom blocks is initiated, $\sigma_{xy}(y = 0)$ is reduced to the sliding friction level, σ^r_{xy}(3.7 MPa), over a slip distance d_c (1.4 μm).

Spontaneous rupture nucleation in friction experiments and in natural faults has been the subject of extensive study (29–32). Previous numerical work has shown that different nucleation procedures can influence the propagating rupture fronts (12, 13, 33, 34). In particular, the more abrupt the initiation, the larger the amplitude of the radiated shear stress peak (13). Here we follow ref. 34 and induce a slowly propagating (~0.1 C_R) initial "seed" crack; starting from $x = 0$, we gradually reduce σ^p_{xy} to σ^r_{xy} over an increasing area. Once the seed crack has reached a critical distance (Griffith length), l_c, rupture acceleration commences and C_f asymptotically approaches C_R as in the example presented in Fig. 3*A*, *Bottom* and Fig. S2.

In Fig. 3*A* a snapshot of σ_{xy} on the interface, $y = 0$, is compared with the simulated field at the height of the experimental measurements, $y = 3.5$ mm. We use these calculations as a basis for quantitative comparison with the experiments. Excellent agreement between the measured $\Delta\varepsilon_{ij}$ and the corresponding numerical calculation (Fig. 3*B*) is obtained. In the numerical simulation, Γ is directly prescribed by the experimental measurements and is not

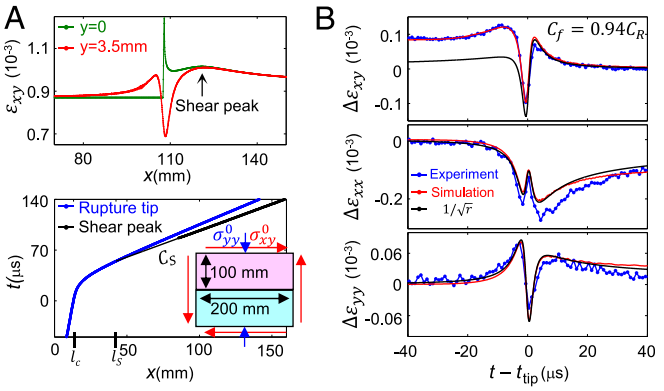

Fig. 3. Finite-element calculations motivated by experiments. (*A*) We mimic the experimental setup by considering spatially homogeneous normal and shear loads (*Bottom*, *Inset*) under quasistatic initiation and loading. The singular rupture tip is regularized by a linear slip weakening cohesive zone model with all parameters experimentally estimated. (*Top*) Simultaneous "snapshots" of the calculated shear component profiles along the interface (green) and at the measurement location $y = 3.5$ mm (red). (*Bottom*) At a critical length, l_c, rapid acceleration to approximately C_R (blue curve) initiates (see text for nucleation procedure). Here, the shear stress peak is well-defined for $x \geq 80$ mm (heavy black curve). Linear extrapolation can be traced back to its initiation point $l_S > l_c$. (*B*) Measured $\Delta\varepsilon_{ij}$ (blue) as a function $t - t_{tip}$ are compared with the corresponding simulation (red). Excellent agreement is observed. Shown in black is the singular term of the LEFM solution ($C_f = 0.94 C_R$, $\Gamma = 1.12$ J/m^2). Whereas Γ is independently measured, C_f is tuned to a value within the experimental error (~2%). Note that the horizontal orientation of the front is reversed, relative to *A*, because the horizontal axis is t instead of x.

an adjustable parameter. The superimposed universal singular solution perfectly describes the calculated $\Delta\varepsilon_{xx}$ and $\Delta\varepsilon_{yy}$ with no additional free parameters, whereas it fails, as was previously discussed, for $\Delta\varepsilon_{xy}$ at $t-t_{tip}<0$. Fig. 3 establishes the reliability of our simulations.

We now use our numerical calculations to provide a detailed description of the shear stress peak structure. We concentrate, first, on the stress field on the interface ($y=0$). Owing to the smooth acceleration of the simulated rupture, the shear stress peak is generally smeared relative to the analytical solution (Fig. 2*A*, *Bottom*) and the numerical calculation (26) of a suddenly expanding shear crack. The shear stress peak can, therefore, not be easily defined at the early stages of rupture propagation, whereas the peak location becomes clear at later stages of its evolution. We define the shear stress peak initiation point by using backward linear extrapolation of the time-position curve of the peak (Fig. 3*A*, *Bottom*). As in the experiments, the shear stress peak consistently initiates at a location, l_S, that is located significantly after the rupture nucleation point, l_c. At this location $C_f\approx 0.85C_R$. These observations are in contrast to the self-similar solution where the shear stress peak initiation point coincides with the rupture nucleation point.

We are now in a position to consider the angular dependence of this propagating stress wave by using the full spatial form of the simulated fields. Two snapshots of the normalized shear strain $\bar{\varepsilon}_{xy}=(\varepsilon_{xy}-\varepsilon^0_{xy})/(\varepsilon^0_{xy}-\varepsilon^r_{xy})$ are plotted in Fig. 4*A*. Because $\varepsilon_{xy}(t,x,y)$ is symmetric with respect to $y=0$, only the upper half-plane is shown. While the rupture front acceleration begins at $x=l_c$, we define polar coordinates (r_S,θ_S) with respect to the initiation point of the stress peak, $x=l_S$. At any moment, r_S is equal to the distance between $x=l_S$ and the current location of the stress peak ($r_S=C_S\Delta t$). The overall maximum of the shear strain concentration ahead of the rupture front is always realized on the interface, $\varepsilon^S_{xy}(r_S)=\varepsilon_{xy}(r_S,\theta_S=0)$ (Fig. 4*A*, *Top*). Its normalized amplitude, $S_S=(\varepsilon^S_{xy}-\varepsilon^0_{xy})/(\varepsilon^0_{xy}-\varepsilon^r_{xy})$, as originally noted in ref. 9, grows with the propagation distance (Fig. 4*B*, *Inset*). To account for this growth, to properly compare the angular form at successive time steps, we plot $\bar{\varepsilon}_{xy}(r_S,\theta_S)$ normalized by S_S in Fig. 4*B*. For small forward angles (up to ~10°), all curves collapse to a single functional form. This collapse suggests a well-defined angular dependence of the stress wave that forms the shear stress peak. We note that this collapse of the angular function is not observed if an origin different from l_S is chosen. Within $\theta_S\sim 5°$ the amplitude is reduced by a factor of 2, implying a very sharp angular dependence. This strong focusing in the direction of the rupture propagation is characteristic of mode II ruptures (2). Such focusing is not present in mode I fracture (35). The difference between the curves for larger angles, we suspect, is due to strong interference with the fields associated with the rupture tip; as the shear stress peak distances itself from the rupture tip the collapse should include an increasingly larger range of angles, as suggested by the approximate approach to an asymptotic angular form in Fig. 4*B*.

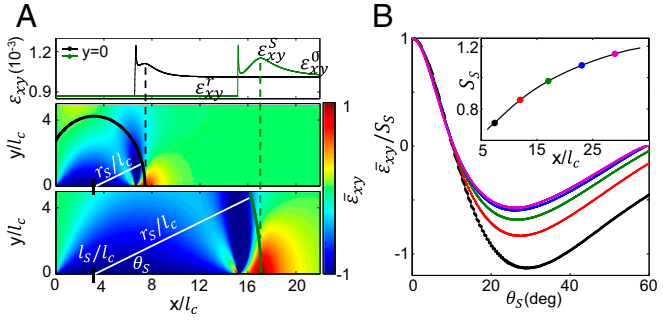

Fig. 4. The angular dependence of the radiated shear stress peak. (*A*) Two snapshots (at different times) of $\bar{\varepsilon}_{xy}=(\varepsilon_{xy}-\varepsilon^0_{xy})/(\varepsilon^0_{xy}-\varepsilon^r_{xy})$. x and y axes are normalized by the Griffith length, l_c. Polar coordinates are defined with their origin at $l_S\approx 3.1l_c$, the initiation point of the shear stress peak (Fig. 3*A*, *Bottom*). θ_S is with respect to the frictional interface. Dashed lines at $r_S=C_S\Delta t$ denote the position of the shear strain peak, ε^S_{xy}, that is always realized along $\theta_S=0$ ($y=0$) (*Upper*). (*B*) The angular dependence in five representative snapshots is compared for different r_S. These strain values are normalized by $S_S=(\varepsilon^S_{xy}-\varepsilon^0_{xy})/(\varepsilon^0_{xy}-\varepsilon^r_{xy})$ (for colors see *Inset*). All curves collapse to a single functional form for small angles up to ~10°, suggesting a well-defined angular functional form for the radiated stress wave that is highly focused around the interface; within $\theta_S\sim 5°$ the amplitude is reduced by 2 (*Inset*). S_S grows with x/l_c. Black and green points correspond to the snapshots in *A*.

Stress-Wave Scaling

Let us now consider what determines the shear stress peak amplitude and scaling. We first consider the effect of preimposed shear stress. Fig. 5*A*, *Left*, *Inset* indicates that the dynamic strain drop, $\varepsilon^0_{xy}-\varepsilon^r_{xy}$, significantly affects the overall amplitude of the shear peak, $\varepsilon^S_{xy}-\varepsilon^0_{xy}$. The larger the values of the dynamic strain drop, the faster the increase in amplitude growth. This suggests that propagation distances should be scaled as well. $l_c\propto(\sigma^0_{xy}-\sigma^r_{xy})^{-2}$ is the sole length scale in the system; all numerical rupture velocity profiles collapse when plotted as a function of x/l_c (Fig. S2) and $l_S\propto l_c$. Fig. 5*A*, *Left* shows that the simulated stress peaks indeed collapse to a single function of the scaled propagation distance x/l_c, $S^S(x/l_c)=(\varepsilon^S_{xy}(x/l_c)-\varepsilon^0_{xy})/(\varepsilon^0_{xy}-\varepsilon^r_{xy})$.

Previous studies had suggested that once the shear stress peak, σ^S_{xy}, reaches the interfacial strength, σ^p_{xy}, a supershear secondary crack is born that propagates above C_S (9) whose transition length has been numerically studied (9, 12–14). In Fig. S3 we show that the observed transition length scaling in refs. 9 and 14 exactly coincides with the growth of $S_S(x/l_c)$ as presented in Fig. 5*A*, *Left*. Although, here, we concentrate on the dynamics of the propagating shear stress peak, we expect that the $S_S(x/l_c)$ scaling exhibited in Fig. 5*A*, *Left* is, therefore, directly relevant to the supershear transition.

How large can $S_S(x/l_c)$ grow? The solutions to the self-similar problem yield S_S values in the range $0<S_S<1.77$ (5). The maximal value, $S^{max}_S\approx 1.77$, corresponds to a sudden velocity jump to C_R whereas $S_S=0$ is the limit when $C_f\to 0$. The value of S^{max}_S might be slightly lower, however, if an asymmetric bilateral crack propagation is considered (5). Our simulations for a smoothly accelerating rupture front show that, when the shear stress peak is first resolved, its minimal value is $S_S\approx 0.7$ (Fig. 5*A*, *Left*). It is expected (9) that S^{max}_S will provide an upper bound; $S_S\to S^{max}_S$ as $x/l_c\to\infty$. Numerically, we are currently limited to an attainable value of $S_S\approx 1.2$; x/l_c is limited because of the need to sufficiently resolve both the system size and the continuously contracting dissipation region (3, 4) as $C_f\to C_R$.

Although the simulations provide us with access to the shear stress peak values at the interface, its sharp angular dependence (Fig. 4*B*) suggests that the experimental estimation of these values at $y=0$ should be performed with some caution. Only for $x\gg l_S$ ($\theta_S\to 0$) will the shear strain measurements performed at $y\approx 3.5$ mm reliably reflect ε^S_{xy} on the interface. To this end, we choose only measurements where $\theta_S<3.5°$ to estimate the shear peak values, $\varepsilon^S_{xy}-\varepsilon^0_{xy}$ ($\theta_S<3.5°$ underestimates peak amplitudes

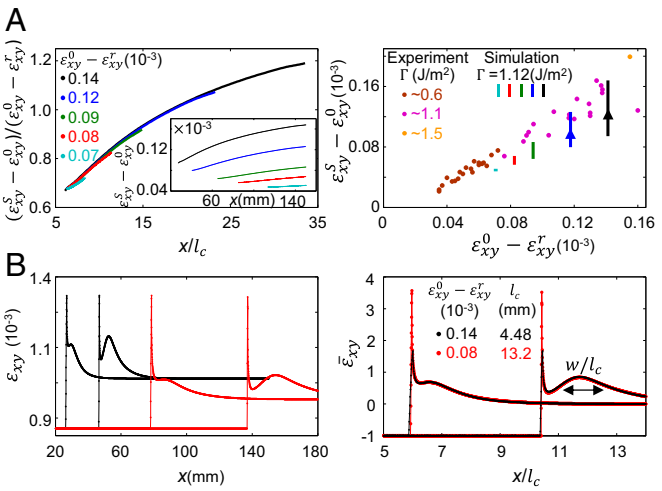

Fig. 5. Scaling of the propagating shear stress peak. (*A*, *Left*) Simulation: shear peak values, $\varepsilon_{xy}^{S}-\varepsilon_{xy}^{0}$, increase in amplitude with both dynamic strain drop $\varepsilon_{xy}^{0}-\varepsilon_{xy}^{r}$ and x. When $\varepsilon_{xy}^{S}-\varepsilon_{xy}^{0}$ is scaled by $\varepsilon_{xy}^{0}-\varepsilon_{xy}^{r}$ and x by l_c all of unscaled curves (*Inset*) collapse to single functional form. Plots are truncated at $x=150$ mm before reflected waves arrive. (*Right*) Experiments indicate that the shear peak amplitude, $\varepsilon_{xy}^{S}-\varepsilon_{xy}^{0}$, roughly scales with $\varepsilon_{xy}^{0}-\varepsilon_{xy}^{r}$. Each solid point corresponds to a single experimental event. Γ varies (see legend) with F_N. Lines corresponding to the numerical growth of shear stress peak amplitude in x are superimposed (colors as in left panel legend; arrows show growth direction). The spread of the measurements is wholly consistent with the growth exhibited in *A*. (*B*) Two examples from the numerical on-fault ($y=0$) waveforms analyzed in *A* (*Left*) demonstrate shear stress peak scaling; waveforms are identical when strain and distance are normalized as in *A* (*Left*). In particular, the width of the wave, w, linearly scales with l_c. $\bar{\varepsilon}_{xy}=(\varepsilon_{xy}-\varepsilon_{xy}^{0})/(\varepsilon_{xy}^{0}-\varepsilon_{xy}^{r})$.

by at most ~20%). These values, presented in Fig. 5*A*, *Right*, are indeed consistent with the numerics (Fig. 5*A*, *Left*) because they convincingly show that the shear peak roughly scales with the dynamic strain drop, $\varepsilon_{xy}^{0}-\varepsilon_{xy}^{r}$. It is, however, difficult to distinguish the numerically observed growth effect (scaling with x) from experimental uncertainties resulting from both spatial stress inhomogeneities and estimation of the measurements for $y=0$. We note that all of the data points in Fig. 5*A*, *Right* fall below the slope $S^{S}=(\varepsilon_{xy}^{S}-\varepsilon_{xy}^{0})/(\varepsilon_{xy}^{0}-\varepsilon_{xy}^{r})\sim 1.3$ and do not reach $S_S^{max}\approx 1.77$. The maximal measured values of S_S may be limited by either the supershear transition or the finite length of the interface. Because this result is specific for the dimensions and applied normal stresses in our system, it may be possible to approach S_S^{max} for a more extended interface.

We further illustrate the scaling of the shear stress peak by considering (Fig. 5*B*) two different simulated rupture events. In each event, two typical snapshots of ε_{xy} on the interface have been chosen. When ε_{xy} and x are properly scaled, the space-time dependence of the on-fault ($y=0$) shear peak waveform collapses to a single function of x/l_c. In particular, its width, w, scales linearly with l_c.

Discussion

We previously (4) demonstrated that the singular functions that were derived to describe shear fracture in the framework of fracture mechanics (7) provide an excellent description of near-tip stress field components—with the notable exception of the shear stress component at high rupture velocities. Here we have shown that this "discrepancy" with the singular solution is not a simple technical issue of accounting for nonsingular contributions to the singular description, but actually possesses a life (and extensive history) of its own.

In contrast to far-field acoustic data (6) that consider a rupture as a moving dipole source, we focused on the near-field radiation emitted by coherent accelerating ruptures. Transporting significant energy ahead of the rupture front, the stress radiation amplitudes can reach the strength of the frictional interface and trigger supershear (5, 9, 11–14). The radiated shear stress peaks have a characteristic near-field signature: high-amplitude radiation (comparable to the dynamic stress drop) that is both localized and strongly focused in the direction of rupture propagation. This signature is a general feature of nonsteady shear rupture (2, 5).

It is significant that both our experiments and simulations show that, during rupture propagation, the shear stress peak does not decrease in amplitude (cf. Fig. 1*B*). In contrast, upon rupture arrest we observe distinct shear stress peak decay (Fig. 1*C*). This decay is consistent with previous theoretical observations (2, 5, 35) of decaying radiation that was associated with abrupt changes of C_f and can be expected from the conservation of radiated energy. A nondecaying stress peak amplitude may therefore be interpreted as due to continuous radiation and transfer of energy from the nonsteady rupture to the propagating shear stress peak. One such example is the self-similar problem, where the rupture does not reach steady-state propagation (27) (although it propagates at constant velocity), because continually increasing amounts of energy are needed to drive constant velocity cracks. On this note, we may attribute the $S_S(x/lc)$ growth presented in Fig. 5 to the asymptotic rupture acceleration to C_R.

How general is the shear stress peak scaling described by Fig. 5? Our simulations considered a particular, although important and fundamental, class of systems: (Griffith-like) quasistatic loading into a uniform initial stress distribution. Many experimental features are well-captured by the simulations (e.g., Figs. 3 and 5), despite the uncontrolled nucleation and ~30% spatial variation of the stresses in the experiments. We, therefore, expect that the peak amplitude and spatial scaling exhibited in Fig. 5 are not critically dependent on small variations of the assumptions used in the simulations. These assumptions may, nevertheless, not hold for a natural fault. In particular, it is known that some nucleation procedures can significantly affect the shear stress peak growth (12, 13, 33, 34). The rupture front's shape during an earthquake may be quite complicated and natural faults are known to be complex entities that include significant heterogeneity of fracture energy, friction laws, stresses, and fault geometry. Even with all of this complexity, however, in some cases (e.g., refs. 17, 36, and 37) qualitative and sometimes quantitative features of natural earthquakes can be both successfully compared with rather idealized models and reproduced in laboratory experiments. Of particular interest are successful comparisons of near-field measurements of quantities such as particle velocities (17, 37). It would be interesting, therefore, to compare near-field measurements of large earthquakes to our results to first determine whether the general features embodied in Fig. 2 are at all apparent. We would expect to see evidence of the shear stress peak followed by the characteristic signature of the singularity at the rupture tip (4), as the rupture passes by the measurement point. These features should be observable both in strain measurements or, as demonstrated in Fig. S1, in particle velocity measurements. If so, measurements at small angles relative to the fault could provide hitherto inaccessible information about both propagating earthquakes and their acceleration phase. For example, the dynamic stress drop, $\sigma_{xy}^{0}-\sigma_{xy}^{r}$ can be roughly approximated by the shear stress peak amplitude—even if one ignores the stress peak amplitude variation with propagation distance. Comparison of this quantity to seismic measurements of the earthquake's overall stress drop would yield information about the contribution to the stress drop by other processes.

ACKNOWLEDGMENTS. We thank G. Cohen for fruitful discussions. This work was supported by James S. McDonnell Fund Grant 220020221, European Research Council Grant 267256, and Israel Science Foundation Grants 76/11 and 1523/15 (all to I.S. and J.F.); European Research Council Grant ERCstg UFO-240332 (to J.-F.M., D.S.K., and D.P.M.); and Swiss National Science Foundation Grant PMPDP2-145448 (to M.R.). This work was also supported by Cornell University (D.S.K.).

1. Burridge R (1973) Admissible speeds for plane-strain self-similar shear cracks with friction but lacking cohesion. *Geophys J R Astron Soc* 35(4):439–455.
2. Madariaga R (1977) High-frequency radiation from crack (stress drop) models of earthquake faulting. *Geophys J Int* 51(3):625–651.
3. Rice JR (1980) The mechanics of earthquake rupture. *Physics of the Earth's Interior*. Proceedings of the International School of Physics "Enrico Fermi", eds Dziewonski AM, Boschi E (North-Holland, Amsterdam), pp 555–649.
4. Svetlizky I, Fineberg J (2014) Classical shear cracks drive the onset of dry frictional motion. *Nature* 509(7499):205–208.
5. Dunham EM (2007) Conditions governing the occurrence of supershear ruptures under slip-weakening friction. *J Geophys Res* 112(B7):B07302.
6. McLaskey GC, Glaser SD (2011) Micromechanics of asperity rupture during laboratory stick slip experiments. *Geophys Res Lett* 38(12):L12302.
7. Freund LB (1990) *Dynamic Fracture Mechanics* (Cambridge Univ Press, New York).
8. Broberg KB (1999) *Cracks and Fracture* (Academic, San Diego).
9. Andrews DJ (1976) Rupture velocity of plane strain shear cracks. *J Geophys Res* 81(32): 5679–5687.
10. Abraham FF, Gao H (2000) How fast can cracks propagate? *Phys Rev Lett* 84(14): 3113–3116.
11. Geubelle PH, Kubair DV (2001) Intersonic crack propagation in homogeneous media under shear-dominated loading: Numerical analysis. *J Mech Phys Solids* 49(3):571–587.
12. Festa G, Vilotte J-P (2006) Influence of the rupture initiation on the intersonic transition: Crack-like versus pulse-like modes. *Geophys Res Lett* 33(15):L15320.
13. Liu Y, Lapusta N (2008) Transition of mode ii cracks from sub-Rayleigh to intersonic speeds in the presence of favorable heterogeneity. *J Mech Phys Solids* 56(2):25–50.
14. Liu C, Bizzarri A, Das S (2014) Progression of spontaneous in-plane shear faults from sub-Rayleigh to compressional wave rupture speeds. *J Geophys Res* 119(11):8331–8345.
15. Psakhie SG, Shilko EV, Popov MV, Popov VL (2015) Key role of elastic vortices in the initiation of intersonic shear cracks. *Phys Rev E Stat Nonlin Soft Matter Phys* 91(6): 063302.
16. Bouchon M, Vallée M (2003) Observation of long supershear rupture during the magnitude 8.1 Kunlunshan earthquake. *Science* 301(5634):824–826.
17. Dunham EM, Archuleta RJ (2004) Evidence for a supershear transient during the 2002 denali fault earthquake. *Bull Seismol Soc Am* 94(6):S256–S268.
18. Rosakis AJ, Samudrala O, Coker D (1999) Cracks faster than the shear wave speed. *Science* 284(5418):1337–1340.
19. Xia K, Rosakis AJ, Kanamori H (2004) Laboratory earthquakes: The sub-Rayleigh-to-supershear rupture transition. *Science* 303(5665):1859–1861.
20. Ben-David O, Cohen G, Fineberg J (2010) The dynamics of the onset of frictional slip. *Science* 330(6001):211–214.
21. Passelègue FX, Schubnel A, Nielsen S, Bhat HS, Madariaga R (2013) From sub-Rayleigh to supershear ruptures during stick-slip experiments on crustal rocks. *Science* 340(6137): 1208–1211.
22. Rubinstein SM, Cohen G, Fineberg J (2007) Dynamics of precursors to frictional sliding. *Phys Rev Lett* 98(22):226103.
23. Radiguet M, Kammer DS, Gillet P, Molinari JF (2013) Survival of heterogeneous stress distributions created by precursory slip at frictional interfaces. *Phys Rev Lett* 111(16): 164302.
24. Kammer DS, Radiguet M, Ampuero JP, Molinari JF (2015) Linear elastic fracture mechanics predicts the propagation distance of frictional slip. *Tribol Lett* 57(3):1–10.
25. Broberg KB (1960) The propagation of a brittle crack. *Ark Fys* 18(2):159–192.
26. Andrews DJ (1985) Dynamic plane-strain shear rupture with a slip-weakening friction law calculated by a boundary integral method. *Bull Seismol Soc Am* 75(1):1–21.
27. Freund LB, Rosakis AJ (1992) The structure of the near-tip field during transient elastodynamic crack growth. *J Mech Phys Solids* 40(3):699–719.
28. Xia K, Chalivendra VB, Rosakis AJ (2006) Observing ideal self-similar crack growth in experiments. *Eng Fract Mech* 73(18):2748–2755.
29. Uenishi K, Rice JR (2003) Universal nucleation length for slip-weakening rupture instability under nonuniform fault loading. *J Geophys Res* 108(B1):2042.
30. Rubin AM, Ampuero J (2005) Earthquake nucleation on (aging) rate and state faults. *J Geophys Res* 110(B11):B11312.
31. Bar-Sinai Y, Spatschek R, Brener EA, Bouchbinder E (2013) Instabilities at frictional interfaces: Creep patches, nucleation, and rupture fronts. *Phys Rev E Stat Nonlin Soft Matter Phys* 88(6):060403.
32. Latour S, Schubnel A, Nielsen S, Madariaga R, Vinciguerra S (2013) Characterization of nucleation during laboratory earthquakes. *Geophys Res Lett* 40(19):5064–5069.
33. Lu X, Lapusta N, Rosakis AJ (2009) Analysis of supershear transition regimes in rupture experiments: The effect of nucleation conditions and friction parameters. *Geophys J Int* 177(2):717–732.
34. Gabriel A-A, Ampuero J-P, Dalguer LA, Mai PM (2012) The transition of dynamic rupture styles in elastic media under velocity-weakening friction. *J Geophys Res* 117(B9):B09311.
35. Rose LRF (1981) The stress-wave radiation from growing cracks. *Int J Fract* 17(1):45–60.
36. Walter JI, et al. (2015) Rupture speed dependence on initial stress profiles: Insights from glacier and laboratory stick-slip. *Earth Planet Sci Lett* 411:112–120.
37. Mello M, Bhat HS, Rosakis AJ, Kanamori H (2014) Reproducing the supershear portion of the 2002 Denali earthquake rupture in laboratory. *Earth Planet Sci Lett* 387:89–96.
38. Read BE, Duncan JC (1981) Measurement of dynamic properties of polymeric glasses for different modes of deformation. *Polym Test* 2(2):135–150.
39. Andrews DJ (1973) A numerical study of tectonic stress release by underground explosions. *Bull Seismol Soc Am* 63(4):1375–1391.
40. Andrews DJ (1999) Test of two methods for faulting in finite-difference calculations. *Bull Seismol Soc Am* 89(4):931–937.
41. Carpenter NJ, Taylor RL, Katona MG (1991) Lagrange constraints for transient finite element surface contact. *Int J Num Met Eng* 32(1):103–128.
42. Tada H, Paris PC, Irwin GR (2000) *The Stress Analysis of Cracks Handbook* (Am Soc Mechanical Engineers, New York), 3rd Ed.